Supplement

Contents:

S1. The MAR model and warming event simulations

MAR is based on the fundamental equations (e.g., mass and momentum conservations) of atmospheric dynamics with the hydrostatic approximation. Its parameterization of turbulence within and above the surface boundary layer uses the Monin–Obukhov similarity theory and the local E–ε model, respectively. The radiative transfer scheme in MAR is the same as in ERA-40 reanalysis (Morcrette, 2002), and also considers the impact of snow particles on atmospheric optical depth. The surface processes follow the "Soil-Ice-Snow-Vegetation-Atmosphere Transfer" scheme. The global reanalysis ERA-Interim (Dee et al., 2011) provides boundary conditions for the regional MAR simulation over the Antarctic plateau. The horizontal resolution is 20 km, and there are 60 vertical levels from the surface up to 10 hPa with a gradual decrease of vertical resolution. The MAR data used in the mercury model are obtained on a horizontal grid of 20 km centered at Dome C. More details of the MAR model are given in the papers by Gallée and colleagues (Gallée and Schayes, 1994; Gallée and Gorodetskaya, 2010; Gallée et al., 2015).

Figure S1 shows the monthly vertical profiles of temperature at Dome C simulated by MAR and Figure S2 shows the monthly vertical profiles of potential temperature simulated by MAR in year 2013. As shown, a convective mixed layer develops during the daytime of the summer months, which may reach about 500 m in Jan and Dec. The vertical turbulent diffusion coefficients (K_z) simulated by MAR in year 2013 are presented in Fig. S3a. The seasonal patterns of K_z are related to those of downward solar radiation (Fig. S3b), with generally higher values in the summer months (Nov–Feb). In summer, significant diurnal variations of K_z and solar radiation are also found. During the non-summer period, warming events occur occasionally, which are generally caused by coastal warm moist air advection over the Antarctic plateau and are accompanied by increasing wind speeds and turbulence (larger K_z values) (Pietroni et al., 2014).

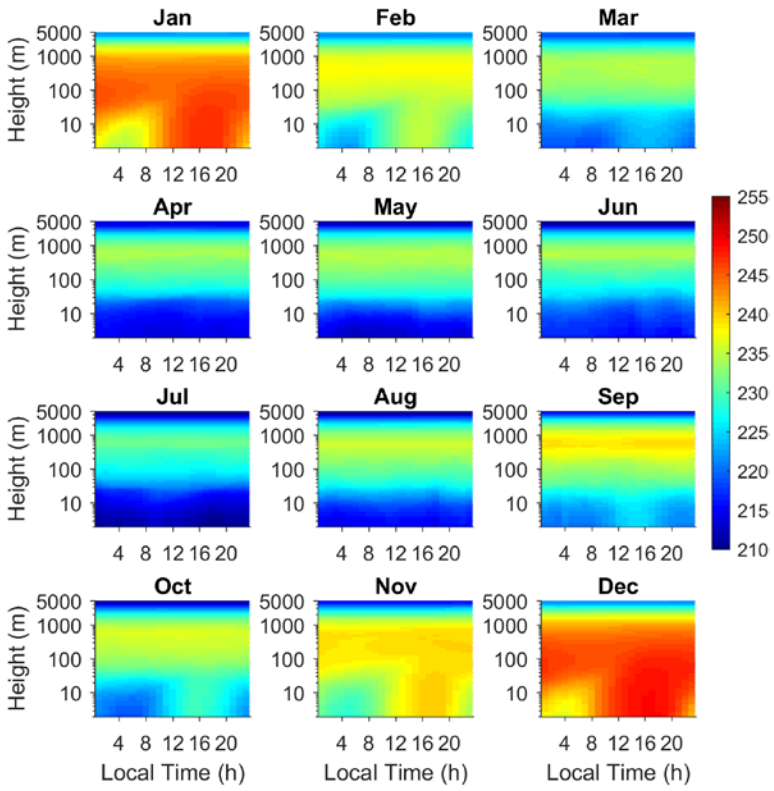

Figure S1. Vertical profiles of temperature (K) modeled by the MAR regional climate model. Each panel shows the average diurnal cycle of temperature for a certain month in year 2013, as indicated in its title. Note that the *y* axis is in log scale.

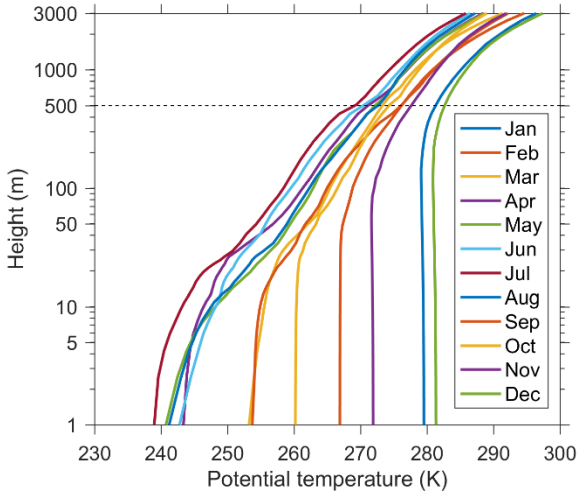

Figure S2. Average monthly vertical profiles of potential temperature (K) modeled by the MAR model at 16:00 local time in year 2013. Note that the *y* axis is in log scale.

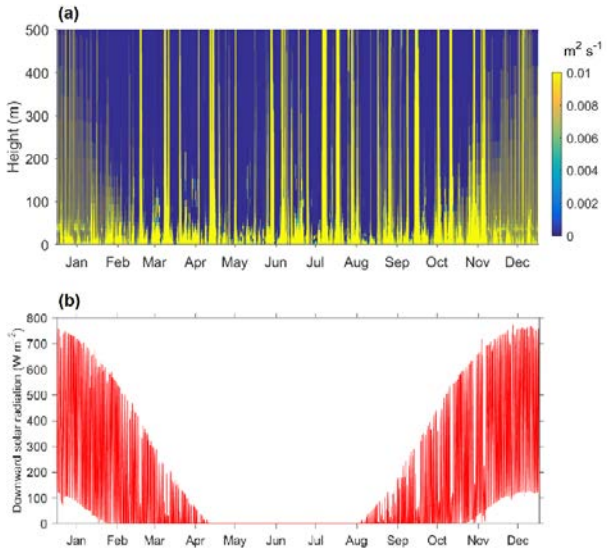

Figure S3. (a) Vertical profiles of K_z from surface up to 500 m and (b) downward solar radiation modeled by MAR in year 2013.

It is important to note that a quantitative understanding of warming events is challenging, and thus large uncertainties exist in their modeling. As shown in Figs. S4 and S5b, the MAR-modeled temperature differences at 42 m and 3.3 m (denoted as ΔT) are commonly small negative values during warming events, whereas the measured ΔT values (from an *in situ* meteorological tower) are usually larger than zero (Genthon et al., 2010). For the non-summer period, the modeled $\Delta T < 0$ occurs about 23% of the time, while the measured $\Delta T < 0$ occurs only about 4% of the time. These comparisons suggest that the strength of warming events is likely overestimated in MAR, which can affect the mercury vertical transport predicted in our box model.

A rough empirical relationship between the modeled values of ΔT and the original K_z can be found, as shown in Fig. S5a. Smaller values of modeled ΔT usually correspond to high K_z values. This relationship is used to tentatively adjust the MAR-modeled K_z values in combination with the observed ΔT values during warming events, using this equation: $K_{z_{adj}}^{i,j} = K_{z_{org}}^{i,j} \cdot \left(f\left(\Delta T_{obs}^{i,3\text{-}42}\right) / K_{z_{org}}^{i,3\text{-}42} \right)$. $K_{z_{adj}}^{i,j}$ and $K_{z_{org}}^{i,j}$ respectively represent the adjusted and original K_z values for the time step i and vertical layer j. $K_{z_{org}}^{i,3\text{-}42}$ are the original K_z values for the time step i, which are averaged between 3.3 m and 42 m. This empirical relationship $K_{z_{org}}^{i,3\text{-}42} = f\left(\Delta T_{mod}^{i,3\text{-}42}\right)$ is inferred from Fig. S5a. $\Delta T_{mod}^{i,3\text{-}42}$ and $\Delta T_{obs}^{i,3\text{-}42}$ are the MAR-modeled and observed temperature differences between 3.3 m and 42 m, respectively (Fig. S4c).

The result of this adjustment is that the values of K_z during warming events are smaller (Fig. S4a–b), indicating weaker exchange between the surface layers and free troposphere. It is important to note that (1) such an adjustment of K_z is subject to large uncertainties since the temperature measurements are only available below 42 m, and (2) the adjusted K_z values tend to underestimate the strength of vertical turbulence since this adjustment applies only to the warming events identified by MAR ($K_{z_{org}}^{3\text{-}42} > 1\ m^2 s^{-1}$) and does not apply to the non-warming events even if the observed ΔT is negative. It is also noted that the choice of K_z values during warming events strongly affects the modeled mercury

concentrations for the non-summer period, and therefore both the original and adjusted K_z values are used to drive the mercury model in this study.

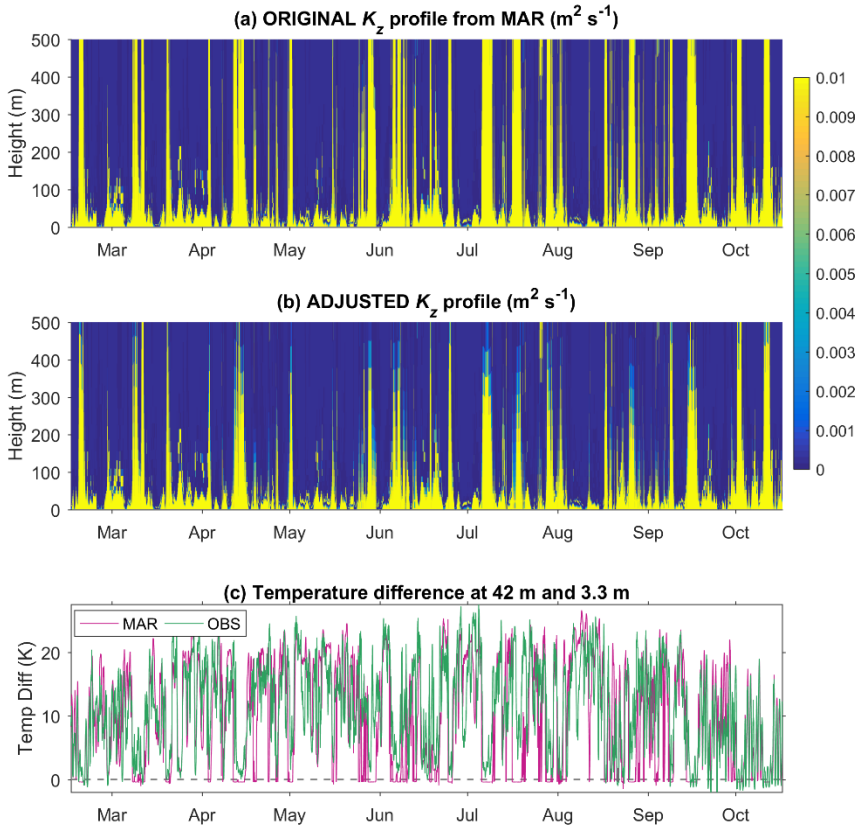

Figure S4. (a) The original MAR-modeled vertical profiles of K_z from surface up to 500 m for the non-summer period (Mar–Oct). (b) The adjusted K_z profile. (c) The observed and modeled temperature difference at 42 m and 3.3 m (ΔT).

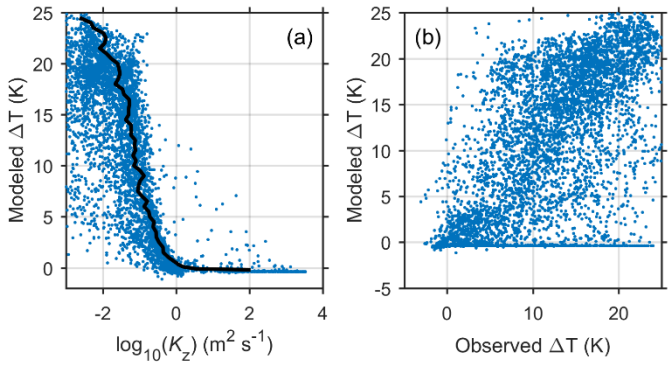

Figure S5. (a) Relationship between MAR-modeled ΔT and original $\log_{10}(K_z)$, which are calculated as the temperature difference and average turbulent coefficients between 42 and 3.3 m, respectively. The black curve indicates the relationship derived from the 75th percentile of $\log_{10}(K_z)$ for each ΔT bin. (b) Relationship between the MAR-modeled and measured ΔT. Data are in an hourly resolution and for the non-summer period (Mar–Oct) in year 2013.

S2. Hg^0 Reaction with other gas-phase oxidants and aqueous/heterogeneous chemistry

The direct gas phase reactions of Hg^0 with several halogen species, NO_x, NO_3, and H_2O_2 are not included in our model because they are unimportant under the conditions of Dome C. Details are given below. **Cl, F, and I.** The oxidation of Hg^0 by these halogen atoms has comparable rate constants with Hg^0 + Br (Donohoue et al., 2005; Dibble et al., 2012). However, Cl also reacts with CH_4, and thus its typical levels are three orders of magnitude lower than Br in the polar regions (Simpson et al., 2007). The levels of F are also very low because it reacts with water vapor (Subir et al., 2011). Hg^{II} is much more unstable than $Hg^{I}Br$ and undergoes thermal dissociation rapidly (Goodsite et al., 2004). **Cl_2, I_2, Br_2, BrCl, ICl, HCl, HOCl, and ClO.** The reactions of Hg^0 with these species have very low rate constants (from 10^{-19} to 10^{-17} cm^3 $molecule^{-1}$ s^{-1}, or even lower) (Subir et al., 2011; Ariya et al., 2015). **F_2.** The rate constant is 1.8×10^{-15} cm^3 $molecule^{-1}$ s^{-1} (Sumner et al., 2005). The F_2 levels are unknown but should be very low given its sources and sinks. **BrO.** The rate constant has been assumed to be from 10^{-15} to 10^{-14} cm^3 $molecule^{-1}$ s^{-1} in several studies, at least 50 times lower than that with Br (Wang et al., 2014; Ye et al., 2016). **NO_x and NO_3.** The oxidation of Hg^0 by NO_x and NO_3 forms unstable products (Dibble et al., 2012), although a positive correlation of Hg^{II} and NO_3 was observed in a case study (Peleg et al., 2015). **H_2O_2.** Given a rate constant of $< 10^{-18}$ cm^3 $molecule^{-1}$ s^{-1} and its levels measured at Dome C, the oxidation of Hg^0 by H_2O_2 is negligible (Kukui et al., 2014; Ariya et al., 2015).

The aqueous and heterogeneous processes are not included in our model primarily due to poor knowledge of their actual mechanisms (Subir et al., 2012). Drifting or blowing snow may provide interfaces for heterogeneous reactions (Libois et al., 2014). However, the presence of aqueous reactions in the cold and dry air at Dome C are unlikely.

S3. Profiles of O_3, HO_x, BrO_x, and NO_x prescribed in our model

Figure S6 shows the monthly and diurnal profiles of O_3, OH, and Br used in our model calculations. The NO_x mixing ratios in ambient air over Dome C are strongly influenced by releases from the surface snow (Frey et al., 2015). Accordingly, it is reasonable to assume that the NO_x concentrations decay from the surface throughout the inversion/mixed layer, which is also consistent with the aircraft observations across the plateau (Slusher et al., 2010). Since near-surface NO_x measurement data are available (Helmig et al., 2018), we can roughly estimate their vertical profiles using the typical chemical lifetimes (τ_{chem}) and vertical turbulent transport time scales (τ_{trans}), as expressed in $C_i = C_1 \cdot \exp(-\tau_{trans}/\tau_{chem})$, where C_i is the NO_x mixing ratios at the ith vertical level and C_1 is the measured mixing ratios at the ground level. τ_{trans} is the time for air to mix vertically from the surface to the ith level and here is calculated from K_z following Jacob (1999). τ_{chem} is the typical NO_x chemical lifetimes on the Antarctic plateau which range from a few hours in summer to several days in winter (Levy et al., 1999; Frey et al., 2015; Zatko et al., 2016). Figure S7 shows the estimated diurnal and monthly vertical profiles of NO_x at Dome C. Figure S8 shows the monthly BrO mixing ratios at Dome C in year 2013 from *p*-TOMCAT and GEOS-Chem. Results from the two CTMs agree well with each other.

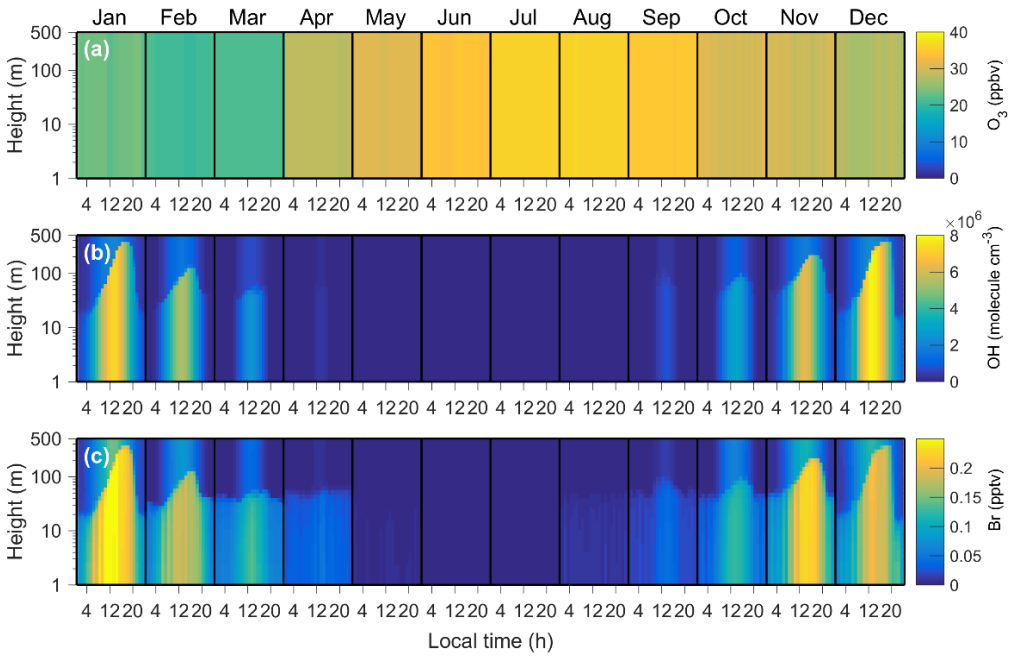

Figure S6. Diurnal variation of monthly average profiles of O_3 (a), OH (b), and Br (c) within the inversion/mixed layer in year 2013. Note that the y axis is in log scale.

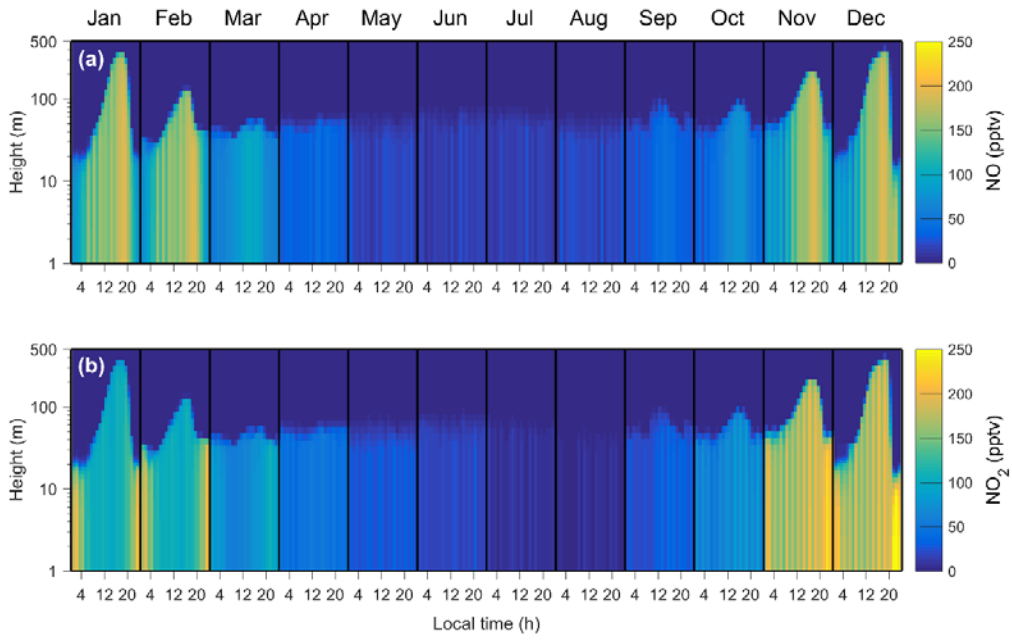

Figure S7. Diurnal variation of monthly average profiles of NO (a) and NO_2 (b) within the inversion/mixed layer in year 2013. Note that the *y* axis is in log scale. In 2013, the near-surface NO_x measurement data in Jan and Dec are missing and thus replaced by those collected in Feb and Nov, respectively; indeed, they are quite comparable to the Dec and Jan observations made at Dome C in previous years (Frey et al., 2013; Frey et al., 2015).

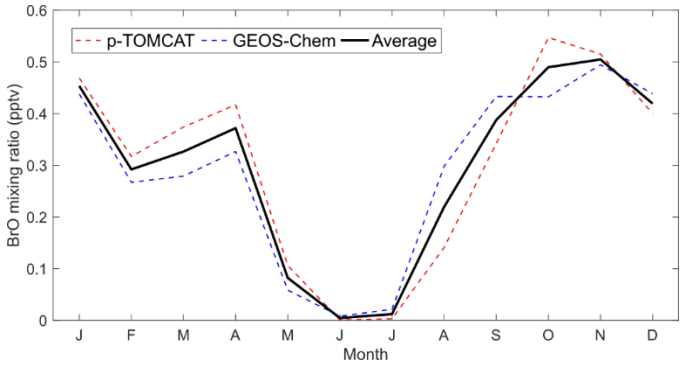

Figure S8. Monthly BrO mixing ratios at Dome C in year 2013. The two dashed lines are the modeling results from *p*-TOMCAT and GEOS-Chem, respectively, which agree well with each other. The black solid line shows the average values of these two models.

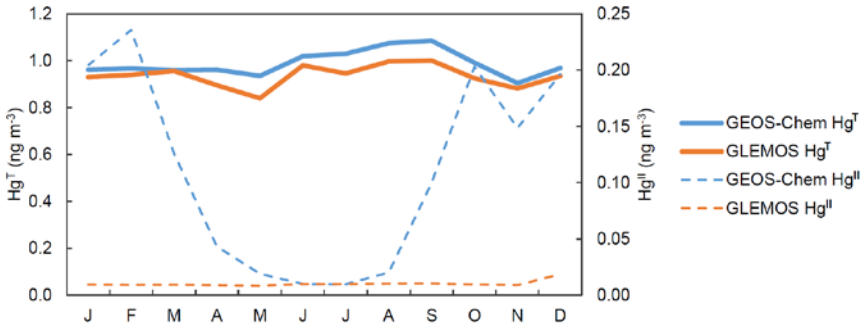

Figure S9. Monthly Hg^T (total mercury) and Hg^{II} concentrations from the GEOS-Chem and GLEMOS global chemical transport models in year 2013. $Hg^0 = Hg^T - Hg^{II}$. For each month, we have adjusted the simulated mercury concentrations in each model using the corresponding factors calculated from the model–observation comparison at Amsterdam Island (38°S 78°E) and Cape Point in South Africa (34°S 18°E), by assuming that these two stations represent the background mercury concentrations in the Southern Hemisphere.

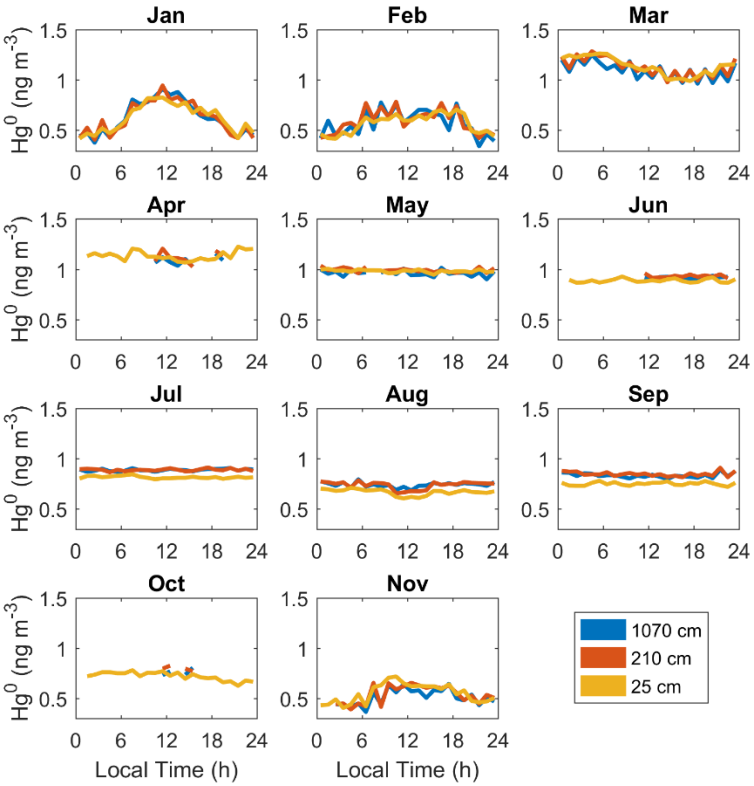

Figure S10. Observed seasonal and diurnal variations of near-surface atmospheric Hg^0 concentrations at different vertical levels (25, 210, and 1070 cm above snow surface) of the meteorological tower at Dome C in year 2013. When deriving the seasonal and diurnal variations of Hg^0, we require > 12 hours data in a day and then > 7 days data in a month. Data for December are not shown here due to fewer available data points.

S4. Comparison of model simulations and observations during summer

In order to evaluate important photochemical processes in the air and surface snow in summer, we conduct a series of model sensitivity simulations by varying atmospheric oxidants (O_3, OH, or Br), their concentrations (high or low), and chemical reaction rates (high or low), and surface snow Hg^{II} photoreduction rates (τ_{PR} from three days to three weeks). The name of each scenario indicates its model setup; for example, O3_HH_3d assumes O_3 as atmospheric oxidant and high oxidant concentrations and high reaction rate constants are applied, and τ_{PR} is set to three days. Figure S10 shows Hg^0 concentrations at different vertical levels (25, 210, and 1070 cm above snow surface), which display similar diurnal patterns in each month, and thus we focus on the model–observation comparisons for the data collected at 25 cm (corresponding to the first vertical atmospheric level in our model). Table S1 lists these 24 model scenarios and quantitative comparisons with near-surface air Hg^0 observations. $NRMSE_D$ and $NRMSE_M$ refer to the normalized root-mean-square errors for the diurnal variation ranges and monthly concentrations of Hg^0 in the summer months, respectively, which are calculated following Song et al. (2015). Figure 3 in the main text and Fig. S11 both show the seasonal and diurnal variations of modeled and observed Hg^0 concentrations in near-surface air.

Table S1. Evaluation of simulation results of different mercury model scenarios in summer.

Name	$NRMSE_D$ (%)	$NRMSE_M$ (%)	Name	$NRMSE_D$ (%)	$NRMSE_M$ (%)
O3_HH_3d	68	106	BR_HL_3d	32	106
O3_HH_7d	66	104	BR_HL_7d	34	98
O3_HH_14d	66	86	BR_HL_14d	41	73
O3_HH_21d	67	71	BR_HL_21d	48	52
OH_HH_3d	71	80	BR_LH_3d	37	104
OH_HH_7d	67	81	BR_LH_7d	19	83
OH_HH_14d	69	76	BR_LH_14d	21	49
OH_HH_21d	71	68	BR_LH_21d	33	27
BR_HH_3d	86	72	BR_LL_3d	66	93
BR_HH_7d	43	36	BR_LL_7d	65	93
BR_HH_14d	**15**	**17**	BR_LL_14d	66	83
BR_HH_21d	27	32	BR_LL_21d	71	71

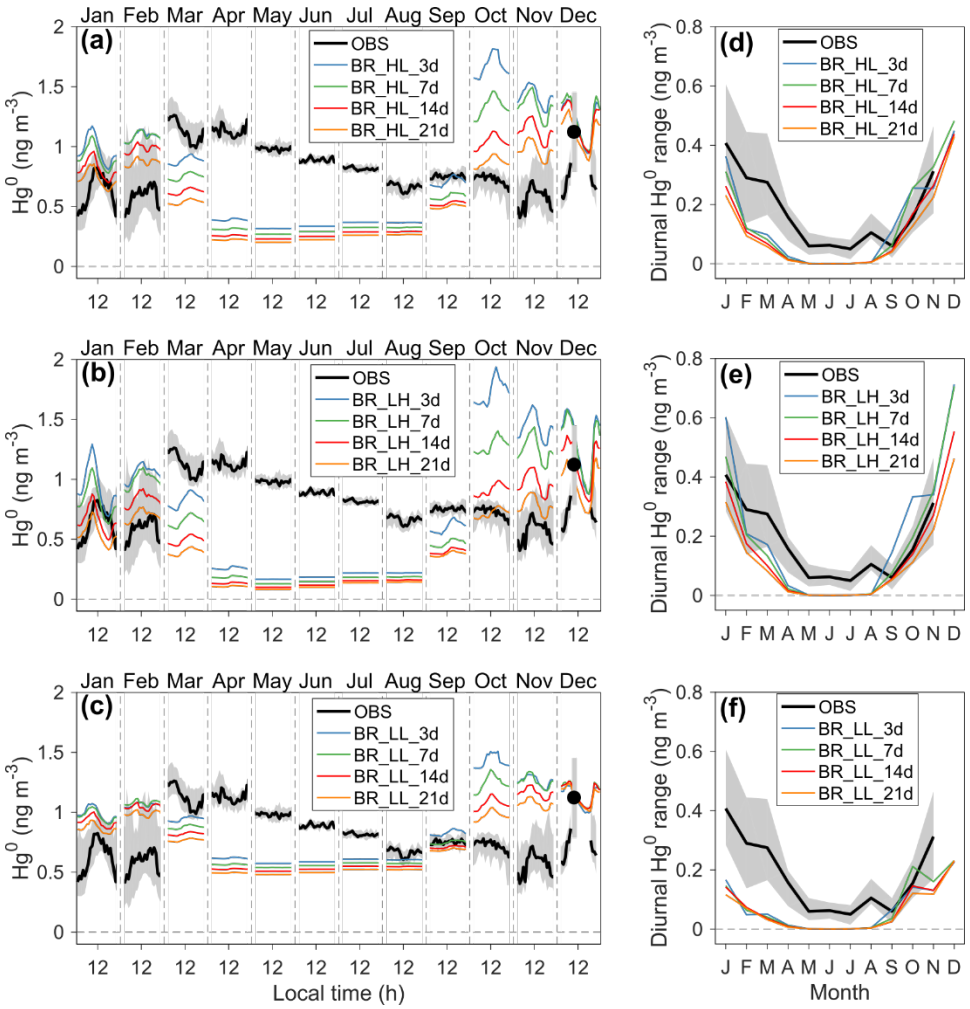

Figure S11. Comparison of seasonal and diurnal variations of near-surface atmospheric Hg^0 concentrations between observations and model. (a–c) show monthly and diurnal Hg^0 observations in year 2013 and modeling results from different scenarios. (d–f) show diurnal Hg^0 ranges calculated from the maximum and minimum hourly concentrations in each month. The shaded regions indicate 25% and 75% percentiles in observations. Observations are conducted at 25 cm above snow at Dome C. The name of each scenario reflects the atmospheric oxidant, its concentration levels and chemical reaction rates (H = *high* or *upper*, L = *low* or *lower*), and the photoreduction rates of snow mercury (in days). For example, the scenario with name "BR_HL_3d" assumes Br as the oxidant, and high oxidant concentrations and low reaction rates are applied, and τ_{PR} is set to three days.

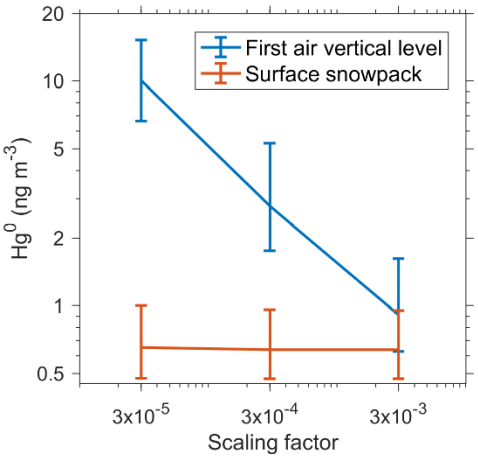

Figure S12. Effects of scaling factors for estimating the turbulent diffusion coefficients (D_t) on the modeled Hg^0 concentrations in the near-surface air and snow interstitial air. Model results from the scenario BR_HH_14d are shown with three different scaling factors (3×10^{-3} s (default value in the model), 3×10^{-4} s, and 3×10^{-5} s). As the scaling factor increases, the values of D_t increase, which means faster vertical turbulent mixing between the air and surface snowpack and thus smaller difference in the modeled Hg^0 concentrations between these two reservoirs.

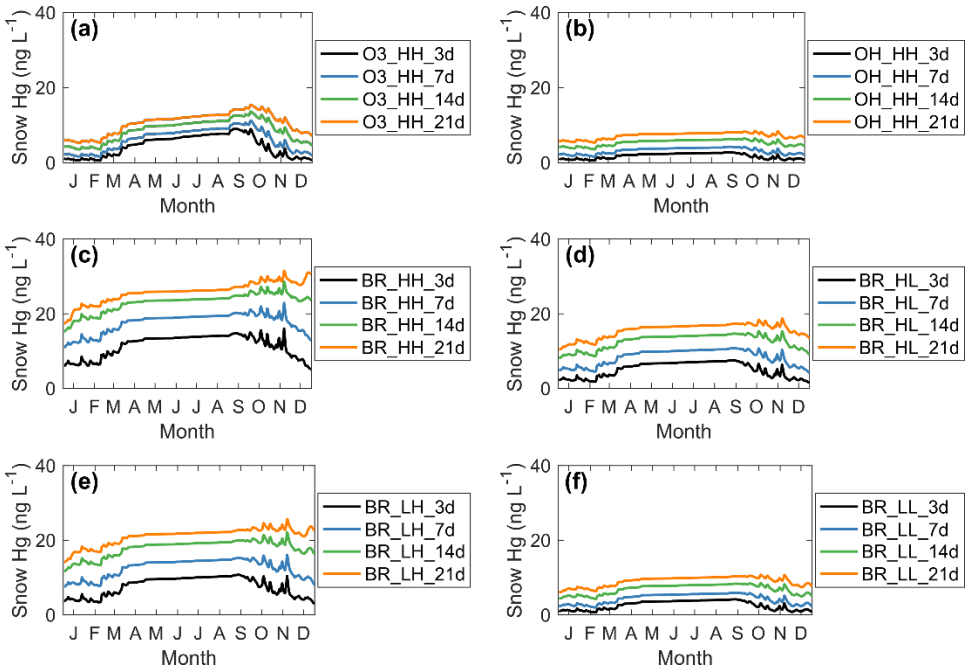

Figure S13. Time series of snow mercury concentrations for different 24 model scenarios.

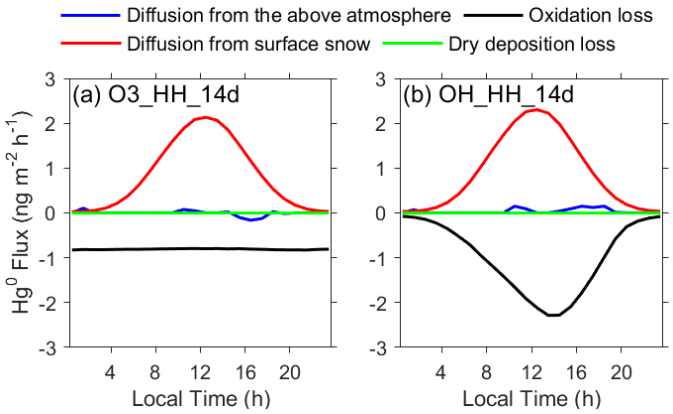

Figure S14. Summertime diurnal cycles of modeled Hg^0 fluxes for the inversion/mixed layers for model scenarios (a) O3_HH_14d and (b) OH_HH_14d.

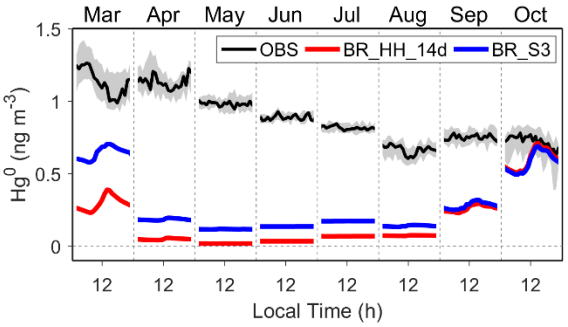

Figure S15. Possible impacts of the overestimation of bromine oxidation on Hg^0 concentrations in the non-summer period. Hg^0 observations at 25 cm above snow at Dome C are shown and the shaded regions indicate 25% and 75% percentiles in observations. The modeled Hg^0 concentrations from BR_HH_14d and BR_S3 are also shown. BR_S3 is a sensitivity simulation (based on BR_HH_14d), in which the BrO concentrations in the fall months (Mar–Apr) are reduced by a factor of 3. The modeled Hg^0 concentrations in the fall and winter months are higher in BR_S3 compared with those in BR_HH_14d.

References

Ariya, P. A., Amyot, M., Dastoor, A., Deeds, D., Feinberg, A., Kos, G., Poulain, A., Ryjkov, A., Semeniuk, K., Subir, M., and Toyota, K.: Mercury physicochemical and biogeochemical transformation in the atmosphere and at atmospheric interfaces: A review and future directions, Chem. Rev., 115, 3760-3802, doi:10.1021/cr500667e, 2015.

Dee, D. P., Uppala, S. M., Simmons, A. J., Berrisford, P., Poli, P., Kobayashi, S., Andrae, U., Balmaseda, M. A., Balsamo, G., Bauer, P., Bechtold, P., Beljaars, A. C. M., van de Berg, L., Bidlot, J., Bormann, N., Delsol, C., Dragani, R., Fuentes, M., Geer, A. J., Haimberger, L., Healy, S. B., Hersbach, H., Hólm, E. V., Isaksen, L., Kållberg, P., Köhler, M., Matricardi, M., McNally, A. P., Monge-Sanz, B. M., Morcrette, J. J., Park, B. K., Peubey, C., de Rosnay, P., Tavolato, C., Thépaut, J. N., and Vitart, F.: The ERA-Interim reanalysis: configuration and performance of the data assimilation system, Q. J. R. Meteorol. Soc., 137, 553-597, doi:10.1002/qj.828, 2011.

Dibble, T. S., Zelie, M. J., and Mao, H.: Thermodynamics of reactions of ClHg and BrHg radicals with atmospherically abundant free radicals, Atmos. Chem. Phys., 12, 10271-10279, doi:10.5194/acp-12-10271-2012, 2012.

Donohoue, D. L., Bauer, D., and Hynes, A. J.: Temperature and pressure dependent rate coefficients for the reaction of Hg with Cl and the reaction of Cl with Cl: A pulsed laser photolysis−pulsed laser induced fluorescence study, J. Phys. Chem. A, 109, 7732-7741, doi:10.1021/jp051354l, 2005.

Frey, M. M., Brough, N., France, J. L., Anderson, P. S., Traulle, O., King, M. D., Jones, A. E., Wolff, E. W., and Savarino, J.: The diurnal variability of atmospheric nitrogen oxides (NO and NO_2) above the Antarctic Plateau driven by atmospheric stability and snow emissions, Atmos. Chem. Phys., 13, 3045-3062, doi:10.5194/acp-13-3045-2013, 2013.

Frey, M. M., Roscoe, H. K., Kukui, A., Savarino, J., France, J. L., King, M. D., Legrand, M., and Preunkert, S.: Atmospheric nitrogen oxides (NO and NO_2) at Dome C, East Antarctica, during the OPALE campaign, Atmos. Chem. Phys., 15, 7859-7875, doi:10.5194/acp-15-7859-2015, 2015.

Gallée, H., and Schayes, G.: Development of a Three-Dimensional Meso-γ Primitive Equation Model: Katabatic Winds Simulation in the Area of Terra Nova Bay, Antarctica, Mon. Weather Rev., 122, 671-685, doi:10.1175/1520-0493(1994)122<0671:doatdm>2.0.co;2, 1994.

Gallée, H., and Gorodetskaya, I. V.: Validation of a limited area model over Dome C, Antarctic Plateau, during winter, Clim. Dyn., 34, 61, doi:10.1007/s00382-008-0499-y, 2010.

Gallée, H., Preunkert, S., Argentini, S., Frey, M. M., Genthon, C., Jourdain, B., Pietroni, I., Casasanta, G., Barral, H., Vignon, E., Amory, C., and Legrand, M.: Characterization of the boundary layer at Dome C (East Antarctica) during the OPALE summer campaign, Atmos. Chem. Phys., 15, 6225-6236, doi:10.5194/acp-15-6225-2015, 2015.

Genthon, C., Town, M. S., Six, D., Favier, V., Argentini, S., and Pellegrini, A.: Meteorological atmospheric boundary layer measurements and ECMWF analyses during summer at Dome C, Antarctica, J. Geophys. Res.-Atmos., 115, doi:10.1029/2009JD012741, 2010.

Goodsite, M. E., Plane, J. M. C., and Skov, H.: A Theoretical Study of the Oxidation of Hg^0 to $HgBr_2$ in the Troposphere, Environ. Sci. Technol., 38, 1772-1776, doi:10.1021/es034680s, 2004.

Helmig, D., Liptzin, D., Hueber, J., and Savarino, J.: Seasonal cycle and snow and atmospheric chemistry of ozone and nitrogen oxides at Concordia Station, manuscript in preparation, 2018.

Jacob, D.: Introduction to atmospheric chemistry, Princeton University Press, 1999.

Kukui, A., Legrand, M., Preunkert, S., Frey, M. M., Loisil, R., Gil Roca, J., Jourdain, B., King, M. D., France, J. L., and Ancellet, G.: Measurements of OH and RO_2 radicals at Dome C, East Antarctica, Atmos. Chem. Phys., 14, 12373-12392, doi:10.5194/acp-14-12373-2014, 2014.

Levy, H., Moxim, W. J., Klonecki, A. A., and Kasibhatla, P. S.: Simulated tropospheric NO x : Its evaluation, global distribution and individual source contributions, J. Geophys. Res.-Atmos., 104, 26279-26306, doi:10.1029/1999JD900442, 1999.

Libois, Q., Picard, G., Arnaud, L., Morin, S., and Brun, E.: Modeling the impact of snow drift on the decameter-scale variability of snow properties on the Antarctic Plateau, J. Geophys. Res.-Atmos., 119, 11,662-611,681, doi:10.1002/2014JD022361, 2014.

Morcrette, J.-J.: Assessment of the ECMWF Model Cloudiness and Surface Radiation Fields at the ARM SGP Site, Mon. Weather Rev., 130, 257-277, doi:10.1175/1520-0493(2002)130<0257:aotemc>2.0.co;2, 2002.

Peleg, M., Tas, E., Obrist, D., Matveev, V., Moore, C., Gabay, M., and Luria, M.: Observational evidence for involvement of nitrate radicals in nighttime oxidation of mercury, Environ. Sci. Technol., 49, 14008-14018, doi:10.1021/acs.est.5b03894, 2015.

Pietroni, I., Argentini, S., and Petenko, I.: One year of surface-based temperature inversions at Dome C, Antarctica, Bound.-Layer Meteor., 150, 131-151, doi:10.1007/s10546-013-9861-7, 2014.

Simpson, W. R., von Glasow, R., Riedel, K., Anderson, P., Ariya, P., Bottenheim, J., Burrows, J., Carpenter, L. J., Frieß, U., Goodsite, M. E., Heard, D., Hutterli, M., Jacobi, H. W., Kaleschke, L., Neff, B., Plane, J., Platt, U., Richter, A., Roscoe, H., Sander, R., Shepson, P., Sodeau, J., Steffen, A., Wagner, T., and Wolff, E.: Halogens and their role in polar boundary-layer ozone depletion, Atmos. Chem. Phys., 7, 4375-4418, doi:10.5194/acp-7-4375-2007, 2007.

Slusher, D. L., Neff, W. D., Kim, S., Huey, L. G., Wang, Y., Zeng, T., Tanner, D. J., Blake, D. R., Beyersdorf, A., Lefer, B. L., Crawford, J. H., Eisele, F. L., Mauldin, R. L., Kosciuch, E., Buhr, M. P., Wallace, H. W., and Davis, D. D.: Atmospheric chemistry results from the ANTCI 2005 Antarctic plateau airborne study, J. Geophys. Res.-Atmos., 115, D07304, doi:10.1029/2009JD012605, 2010.

Song, S., Selin, N. E., Soerensen, A. L., Angot, H., Artz, R., Brooks, S., Brunke, E. G., Conley, G., Dommergue, A., Ebinghaus, R., Holsen, T. M., Jaffe, D. A., Kang, S., Kelley, P., Luke, W. T., Magand, O., Marumoto, K., Pfaffhuber, K. A., Ren, X., Sheu, G. R., Slemr, F., Warneke, T., Weigelt, A., Weiss-Penzias, P., Wip, D. C., and Zhang, Q.: Top-down constraints on atmospheric mercury emissions and implications for global biogeochemical cycling, Atmos. Chem. Phys., 15, 7103-7125, doi:10.5194/acp-15-7103-2015, 2015.

Subir, M., Ariya, P. A., and Dastoor, A. P.: A review of uncertainties in atmospheric modeling of mercury chemistry I. Uncertainties in existing kinetic parameters – Fundamental limitations and the importance of heterogeneous chemistry, Atmos. Environ., 45, 5664-5676, doi:10.1016/j.atmosenv.2011.04.046, 2011.

Subir, M., Ariya, P. A., and Dastoor, A. P.: A review of the sources of uncertainties in atmospheric mercury modeling II. Mercury surface and heterogeneous chemistry – A missing link, Atmos. Environ., 46, 1-10, doi:10.1016/j.atmosenv.2011.07.047, 2012.

Sumner, A. L., Spicer, C. W., Satola, J., Mangaraj, R., Cowen, K. A., Landis, M. S., Stevens, R. K., and Atkeson, T. D.: Environmental Chamber Studies of Mercury Reactions in the Atmosphere, in: Dynamics of Mercury Pollution on Regional and Global Scales:: Atmospheric Processes and Human Exposures Around the World, edited by: Pirrone, N., and Mahaffey, K. R., Springer US, Boston, MA, 193-212, 2005.

Wang, F., Saiz-Lopez, A., Mahajan, A. S., Gómez Martín, J. C., Armstrong, D., Lemes, M., Hay, T., and Prados-Roman, C.: Enhanced production of oxidised mercury over the tropical Pacific Ocean: a key missing oxidation pathway, Atmos. Chem. Phys., 14, 1323-1335, doi:10.5194/acp-14-1323-2014, 2014.

Ye, Z., Mao, H., Lin, C. J., and Kim, S. Y.: Investigation of processes controlling summertime gaseous elemental mercury oxidation at midlatitudinal marine, coastal, and inland sites, Atmos. Chem. Phys., 16, 8461-8478, doi:10.5194/acp-16-8461-2016, 2016.

Zatko, M., Geng, L., Alexander, B., Sofen, E., and Klein, K.: The impact of snow nitrate photolysis on boundary layer chemistry and the recycling and redistribution of reactive nitrogen across Antarctica and Greenland in a global chemical transport model, Atmos. Chem. Phys., 16, 2819-2842, doi:10.5194/acp-16-2819-2016, 2016.